

² **Commissioning and performance in beam tests of the**
³ **highly granular SiW-ECAL technological prototype for the**
⁴ **ILC**

⁵ *E-mail:* irles@lal.in2p3.fr

⁶ **ABSTRACT:** High precision physics at future colliders as the International Linear Collider (ILC)
⁷ require unprecedented high precision in the determination of the final state of the particles produced
⁸ in the collisions. The needed precision will be achieved thanks to the Particle Flow algorithms (PF)
⁹ which require compact, highly granular and hermetic calorimeters systems. The Silicon-Tungsten
¹⁰ Electromagnetic Calorimeter (SiW-ECAL) technological prototype design and R&D is tailored to
¹¹ the baseline design of the ECAL of the International Large Detector (ILD) for the ILC. In this
¹² document we present and discuss the commissioning of the prototype and the performance of the
¹³ device in a beam test carried at DESY in June 2017.

¹⁴ **KEYWORDS:** Calorimeter methods, calorimeters, Si and pad detectors

15	Contents	
16	1 Introduction	1
17	2 The SiW-ECAL technological prototype	3
18	2.1 Silicon sensors	3
19	2.2 SKIROC: Silicon pin Kalorimeter Integrated ReadOut Chip	4
20	2.3 Active Sensor Units	4
21	2.4 Data AcQuisition system	5
22	2.5 Readout layers and SLABs	6
23	3 Commissioning	6
24	3.1 Optimization of noise levels	7
25	3.2 Threshold determination	8
26	3.3 S/N ratio in the trigger line	10
27	3.4 Prospects	11
28	4 Performance on positron beam test at DESY	13
29	4.1 Response to MIP-acting positrons	14
30	4.1.1 Pedestal and noise determination	14
31	4.1.2 Energy calibration and tracking efficiency	15
32	4.1.3 S/N ratio in the charge measurement for MIP interactions	17
33	4.2 Pedestal and noise stability in a magnetic field	17
34	4.3 Pedestal stability in electromagnetic shower events	17
35	5 Summary	19
36	6 Outlook	19
37	A Appendix: Filtering of fake triggers	21

38 **1 Introduction**

39 Future accelerator based particle physics experiments require very precise and detailed reconstruc-
40 tion of the final states produced in the beam collisions. A particular example is the next generation
41 of e^+e^- linear colliders such the ILC[1–5]. This project will provide collisions of polarized beams
42 with centre-of-mass energies (*c.m.e*) of 250 GeV - 1 TeV. These collisions will be studied by two
43 multipurpose detectors: the International Large Detector (ILD) and the Silicon Detector (SiD)[5].
44 Another example of an e^+e^- collider project is the Compact Linear Collider (CLIC) project[6–8]
45 which will produce collisions with *c.m.e* of 380 GeV - 3 TeV with a detector featuring similar

46 design than the ILD and SiD. Both projects will explore with unprecedented precision the origin of
47 the electroweak symmetry breaking and new physics beyond the standard model by exploring final
48 states with heavy bosons (W , Z and H) and fermions (*i.e.* heavy quarks as c , b and t).

49 It is known that in a *classical* typical multipurpose detector of a collider experiment the
50 charged particles momentum is better measured by the tracking system the photons energy are only
51 observed in the calorimeter system (mainly in the electromagnetic) if they are not converted and
52 the measurement of the neutral hadrons energy can only be done by involving the full calorimeter
53 systems. To meet the required precision levels by the ILC or CLIC physics goals, new techniques
54 relying on single particle separation to make possible the choice of the best information available
55 in the full detector to measure the energy of the final state objects have been developed. These
56 techniques are called Particle Flow (PF) techniques [9–11] and allow to reduce the impact of the
57 poor resolution of the calorimeter systems (compared with trackers) in the overall reconstruction.
58 For this purpose, detectors optimized for PF algorithms have some requirements. Some of them are
59 summarized here:

- 60 • a highly efficient and "transparent" tracking system between the interaction point and the
61 calorimetry systems;
- 62 • highly granular (*imaging calorimetry*) and compact calorimeter systems featuring minimum
63 dead material;
- 64 • and high power of particle separation¹.

65 The R&D of highly granular calorimeters for future linear colliders is conducted within the
66 CALICE collaboration and, for now on, we refer the reader to [11] for further information about PF
67 and the CALICE R&D.

68 In this document we will focus in the description of the silicon-tungsten electromagnetic
69 calorimeter, SiW-ECAL, its commissioning and its performance in beam test. The SiW-ECAL is
70 the baseline choice for the ILD ECAL. It consists in a detector (in the barrel region) of $24 X_0$ of
71 thickness which corresponds to $\sim 1 \lambda_I$ (interaction length). It has silicon (Si) as active material and
72 tungsten (W) as absorber material. The combination of Si and W choices makes possible the design
73 and construction of a very compact calorimeter with highly granular and compact active layers.
74 It will consist of an alveolar structure of carbon fiber into which modules called SLABs made of
75 tungsten plates and the active sensors will be inserted. The very-front-end (VFE) electronics will
76 be embedded in the SLABs. The silicon sensors will be segmented in squared cells (or channels)
77 of 5×5 mm: a total of ~ 100 million channels will constitute the ECAL for ILD. The desired
78 signal dynamic range in each channel goes from 0.5 MIP to 3000 MIPs. To reduce overall power
79 consumption, the SiW-ECAL will exploit the special bunch structure foreseen for the ILC: the e^+e^-
80 bunches trains will arrive within acquisition windows of $\sim 1\text{--}2$ ms width separated by ~ 200 ms.
81 During the idle time, the bias currents of the electronics will be shut down. This technique is usually
82 denominated power pulsing. In addition to this, to cope with the large amount of channels, the

¹ For that reason the calorimeter systems at ILD will be placed inside the magnetic coil providing magnetic fields of 3.5 T

83 calorimeters should work in self-trigger mode (each channel featuring an internal trigger decision
84 chain) and zero suppression mode.

85 The first SiW-ECAL prototype was the so called SiW-ECAL physics prototype. It was suc-
86 cessfully tested at DESY, FNAL and CERN running in front of another prototype from the CALICE
87 collaboration, the analogue hadronic calorimeter AHCAL, delivering the proof of concept of the
88 technology and the PF calorimetry. For the physics prototype, the VFE was placed outside the
89 active area with no particular constraints in power consumption. It consisted of 30 layers of Si as
90 active material alternated with tungsten plates as absorber material. The active layers were made
91 of a matrix of 3x3 Si wafers of 500 μm thickness. Each of these wafers was segmented in matrices
92 of 6x6 squared channels of 1x1 cm^2 , allowing for density of 1500 channels/dm³. The prototype was
93 divided in 3 modules of 10 layers with different W depth per layer in each of these modules (0.4,
94 1.6 and 2.4 X_0) making a total of 24 X_0 . That very first prototype offered a signal over noise on the
95 measured charge of 7.5 for MIP like particles. More results proving the good performance of the
96 technology and the PF can be found in references [12–17].

97 2 The SiW-ECAL technological prototype

98 The new generation prototype is called the SiW-ECAL technological prototype. It addresses the
99 main technological challenges: compactness, power consumption reduction through power pulsing
100 and VFE inside the detector close to real ILD conditions. It will also provide data to deeply study
101 the PF and provide input to tune simulation programs as for example GEANT4[18–20] which is
102 widely used in particle physics to simulate the passage of particles through matter.

103 2.1 Silicon sensors

104 The sensors consist on floating zone silicon wafers 320 μm thick with high resistivity (bigger than
105 5000 $\Omega\cdot\text{cm}$). The size of the wafer is $9 \times 9 \text{ cm}^2$ and it is subdivided in an array of 256 PIN diodes
106 of $5 \times 5 \text{ mm}^2$. A MIP traversing the PIN parallel to its normal will create $\sim 80 h^+e^-$ pairs per μm
107 which corresponds to 4.1 fC for particles incident perpendicularly to its surface.

108 The original design of the silicon wafers included an edge termination made of floating guard-
109 rings. It was observed in beam tests [21, 22] that the capacitive coupling between such floating
110 guard-rings and the channels at the edge was not negligible in tests with high energy beams (pions
111 and electrons with energies larger than 20-40 GeV). This coupling lead to fake events in which,
112 at least, the channels in the four edges of the wafer are triggered at the same time. This is why
113 these events are called squared events. An R&D program together with Hamamatsu Photonics
114 (HPK Japan) was conducted to study the guard-rings design as well as the internal crosstalk. It
115 was concluded that using wafers without guard rings and with a width of the peripheral areas lower
116 than 500 μm thanks to the use of stealth dicing technique, the amount of these squared events can
117 be reduced to be almost negligible. This need to be confirmed in beam test. Unfortunately, for the
118 interaction with low energy particles as the delivered at the DESY beam test facility (see Section 4)
119 the amount of squared events is expected to be negligible, therefore we will not discuss this issue
120 in the following.

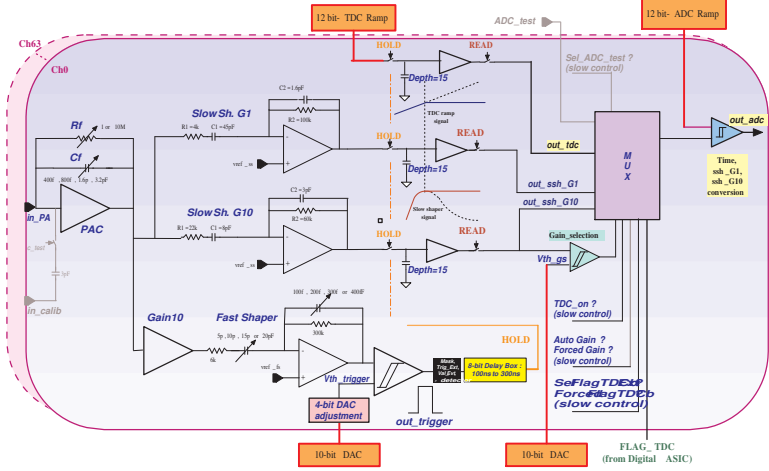


Figure 1. The schematics of the analog part of SKIROC2. High-stack picture (right bottom corner)

121 2.2 SKIROC: Silicon pin Kalorimeter Integrated ReadOut Chip

122 The SKIROC[23] (Silicon pin Kalorimeter Integrated ReadOut Chip) is a very front end ASIC
 123 (application-specific integrated circuits) designed for the readout of the Silicon PIN diodes. In its
 124 version SKIROC2 it consists of 64 channels in AMS 0.35 μm SiGe technology. Each channel
 125 comprises a low noise charge preamplifier of variable gain followed by two branches: a fast shaper
 126 for the trigger decision and a set of dual gain slow shaper for charge measurement. The gain can
 127 be controlled by modifying the feedback capacitance during the configuration of the detector. With
 128 the slowest gain, 6pF, the ASIC will handle a linear dynamic range from 0.1 to up to 1500 MIPs
 129 (a slightly less than the desired final value for the ILC). Finally, a Wilkinson type analogue to
 130 digital converter fabricates the digitized charge deposition that can be readout. Once one channel is
 131 triggered, the ASIC reads out all 64 channels adding a bit of information to tag them as triggered or
 132 not triggered and the information is stored in 15 cell deep physical switched capacitor array (SCA).

133 The SKIROC ASICs can be power-pulsed by taking advantage of the ILC spill structure: the
 134 bias currents of the ASIC can be switched off during the idle time between bunch trains. With this
 135 method, the ASIC is able to reduce its power consumption down to 25 μW per channel, meeting
 136 the ILC requirements. All the results shown in this paper are obtained in power pulsing mode.

137 2.3 Active Sensor Units

138 The entity of sensors, thin PCB (printed circuit boards) and ASICs is called Active Signal Units or
 139 ASU. An individual ASU has a lateral dimension of 18x18 cm². The ASUs are currently equipped
 140 further with 16 SKIROC2 ASICs for the read out and features 1024 square pads (64 per ASIC) of
 141 5x5 mm. The channels and ASICs are distributed along the ASU as shown in Figure 2. Each ASU
 142 is equipped with 4 silicon wafers as the described in Section 2.1. The high voltage is delivered to
 143 the wafers using a HV-kapton sheet that covers the full extension of the wafers.

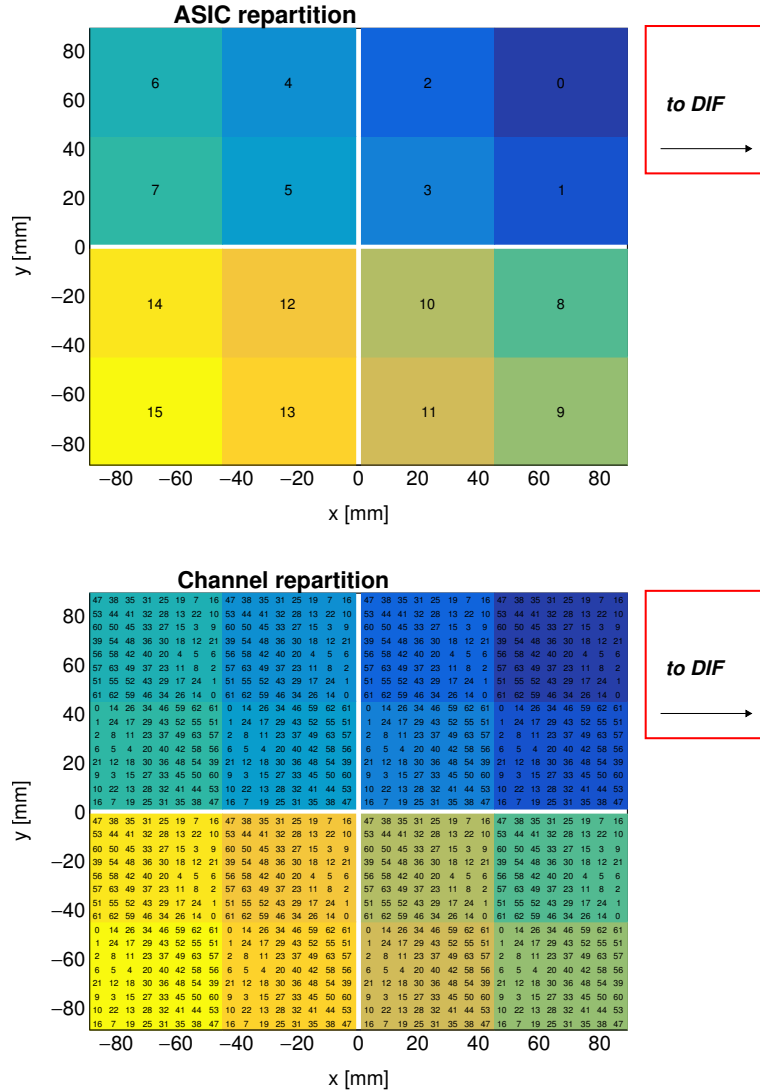


Figure 2. Repartition of the ASIC (up) and channels (down) in one ASU. In this perspective, the Si-Sensors are glued in the back. The channels are separated (in x and y) by 5.5 mm. The empty cross in the middle of the ASU corresponds to the 1 mm separation between the sensors. The areas covered by the different ASICs and channels are labeled with numbers following design and DAQ criteria: from 0-16 in the case of the ASICs and from 0-63 in the case of the channels.

2.4 Data AcQuisition system

The subsequent chain of the data acquisition (DAQ)[24] system is inspired by the ILC. It consists on three modules. The first module is the so called detector interface (DIF) which is placed at the beginning of each layer holding up to 15 ASUs; All DIFs are connected by single HDMI cables to the concentrator cards that make the second module: the Gigabit Concentrator Cards (GDCCs). This cards are used to control up to 7 DIFs collecting all data from them and distributing among them the system clock and fast commands. The last module, the most downstream, is the clock and control card (CCC) which provides a clock, control fan-out of up to 8 GDCCs and accepts and



Figure 3. Temporary picture: La Esperanza del Condenado, J. Miró: Open single SLAB with FEV11 ASU, 16 SKIROC 2, interface card and DIF visibles.

152 distributes external signals (i.e. signals generated by external pulse generator to simulate the ILC spill
 153 conditions). The whole system is controlled by the Calicoes and the Pyrame DAQ software version
 154 3 [25, 26].

155 2.5 Readout layers and SLABs

156 The readout layers of the SiW-ECAL consist of a chain of ASUs and an adapter board to a data
 157 acquisition system (DAQ) at the beginning of the layer. This adapter board is called SMBv4 and it
 158 also serves as to hold other services as power connectors or the super capacitances used for the power
 159 pulsing. These capacitances of 400mF with $16\text{ m}\Omega$ of equivalent serial resistance. The purpose of
 160 these capacitances is to provide local storage of the necessary charge to avoid the transport of current
 161 pulses over long cables, ensuring in this way the stability of the ASICs during the acquisition.

162 The readout layers are embedded on a "U" shape carbon structure to protect the wafers. The full
 163 system is then covered by two aluminum plates to provide electromagnetic shielding and mechanical
 164 stability. This ensemble is denominated SLAB ("short" for 1 ASU ensembles or "long" for several
 165 ASUs enchain) and it can be seen in Figure 3. With current SLABs, a potential density of
 166 $4000\text{ channels}/\text{dm}^3$ is achievable. This number should be compared with the density achieved for
 167 previous beam tests: $1500\text{ channels}/\text{dm}^3$ [27].

168 The SiW-ECAL detector designed for the ILD requires of the order of 10^5 highly integrated
 169 detection like the ones described in this text. For the production of the small sample of SLABs
 170 studied in this document, a scalable working procedure has been established among several groups
 171 [28] profiting from the funding of projects like AIDA2020 or the HIGTEC emblematic project of
 172 the P2IO. A schematic view of this assembly procedure chain can be seen in Figure 4. For more
 173 details we refer to Ref.[28].

174 3 Commissioning

175 This beam test was prepared by a careful and comprehensive commissioning comprising the debug
 176 of the short SLABs with special emphasis in the control of the noise and the study of the prototype
 177 performance in cosmic rays tests.

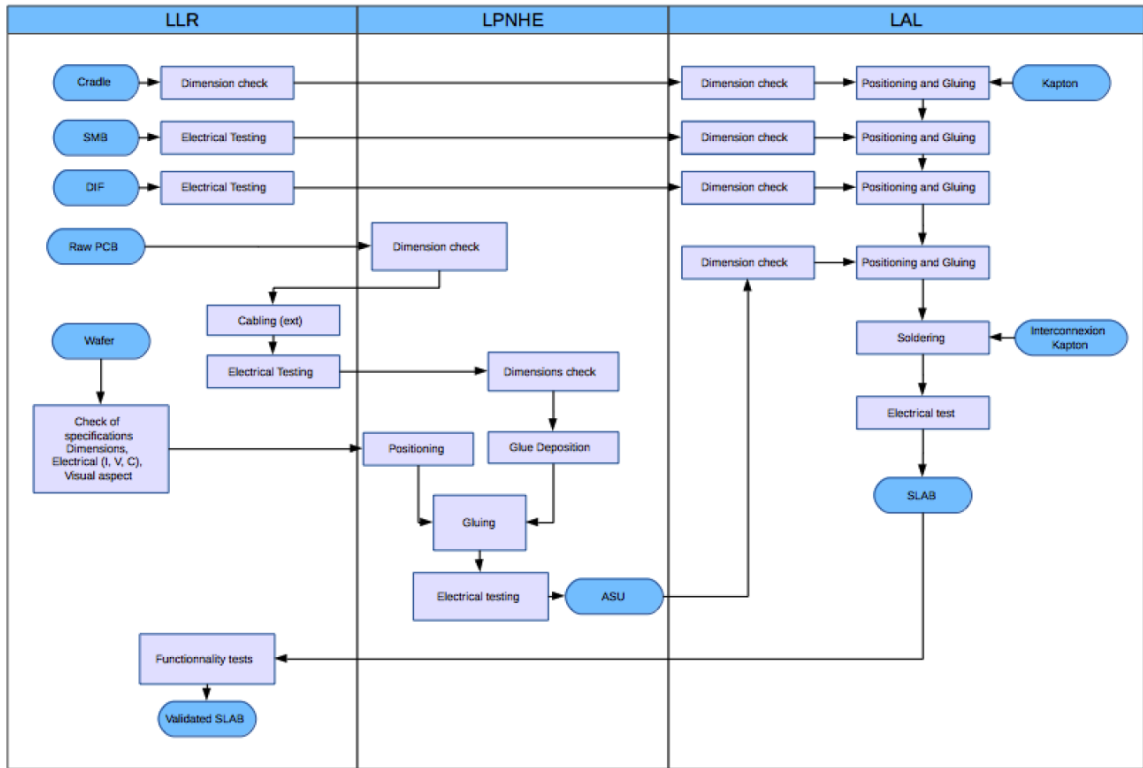


Figure 4. Process flow for the assembly of the SiW-ECAL SLABS.

178 Earlier experiences with the SKIROC2 ASIC are reported in Refs. [27, 29]). Internal SKIROC2
 179 parameters found in these references are adopted in the following except if the opposite is stated.
 180 For example, the gain value of 1.2pF for the preamplifier is used. With this gain, the SKIROC2
 181 ensures a linearity better than 90% for 0.5-200 MIPs, which is enough for electromagnetic showers
 182 created by few GeV electrons or positrons.

183 3.1 Optimization of noise levels

184 Studying and control the noise levels is crucial since noisy channels may saturate the DAQ faster
 185 than physical signals. Two different types of noise sources were identified: a set of noisy channels
 186 randomly distributed in time and noise bursts affecting to all layers at the same time. The outcome
 187 of this commissioning is summarized in Figure 5.

188 The first type of noise source, noise events randomly distributed in time, forced us to define a
 189 list of channels to be masked in all layers. Again, two different type of noisy channels have been
 190 identified. The first group is composed by randomly distributed in space channels. The second group
 191 is made of a fixed list of channels, all in the same positions for all SLABs, and all associated to a
 192 higher rate of events with underflowed value of the read ADC. A large amount of these channels are
 193 located in areas of the PCB where the density of lines (data and power transmission) is higher than
 194 in others. This hints for an issue on the routing of the PCB. Therefore, these channels are tagged
 195 in Figure 5 with the "routing issues" label although more tests and deeper inspections of the PCB
 196 layout are needed to clarify this issue.

197 The list of the noisy channels randomly distributed in time and space was defined by means
 198 of dedicated data taking runs. These runs were characterized by: their short acquisition windows
 199 (open to data recording for only 1.1 ms) at low repetition frequencies (5 Hz) to minimize the chances
 200 of having real events due to cosmic rays hitting the detector during the data taking; and the relatively
 201 high trigger threshold values between 250 and 400 DAC (which are equivalent to ~0.5-2 MIP, see
 202 Section 3.2 for more information). The full process was an iterative process starting with several
 203 repetitions of runs at a high threshold value and then some iterations at lower threshold but always
 204 higher than 0.5 MIP. In each of the iterations, the channels identified as noisy were masked. A full
 205 run involved 3-5 threshold values and at least two repetitions per value. Again, we decided to follow
 206 a conservative approach for list the noisy channels to be masked: if the channel was triggered at
 207 rates larger than 0.5-1% of the total number of triggers per ASIC it was added to the list. These
 208 channels are labeled as "other" in the first plot in Figure 5.

209 In addition to the different noisy channel types described above, we also have masked full
 210 sectors of the SLABs if an ASIC was faulty (at least 70% of channels listed as noisy) or if a Si-wafer
 211 was misworking (high leakage currents). In these cases and in all mentioned above, the masking
 212 involved two steps: disabling of the trigger and the disabling of the power of the preamplifier of
 213 that channel.

214 The other source of noise mentioned at the beginning of this section consist on noise bursts
 215 happening coherently at the same time in all SLABs and it was correlated to occasions when the
 216 electrical isolation between SLABs was broken. This is a hint of a system effect as can be the
 217 appearance of grounding loops or disturbances in the power supplies. The issue was circumvented
 218 by improving the electrical isolation of single layers. We have also observed that the noise bursts
 219 happens only at the end of long acquisitions. Therefore, in addition to the improved isolation, we
 220 selected short enough acquisitions windows (which indeed are the most appropriate to the high
 221 rates of particles in the DESY beam). Ddicated studies in the laboratory are currently pongoingin
 222 order to fully understand this issue.

223 The list of channels mentioned above is discarded from the data taking from now on.

224 3.2 Threshold determination

225 In order to select the optimal trigger threshold values for the detector operation we perform dedicated
 226 scans of trigger threshold values with all channels enabled (excepted the marked as noisy). The
 227 threshold values are given in internal DAC units which are translated to meaningful physical
 228 quantities in Section 3.3. The threshold scan curves made of the total number of hits normalized
 229 to 1 vs the threshold for each channel are modeled by a complementary error function called ThS
 230 curves from now on:

$$ThS(DAC) = p_0 \times erfc\left(\frac{DAC - p_1}{p_2}\right) = \frac{2p_0}{\sqrt{\pi}} \int_{\frac{DAC-p_1}{p_2}}^{\infty} e^{-t^2} dt, \quad (3.1)$$

231 where p_0 is 1/2 of the normalization, p_1 is the value in which the noise levels are the 50% of its
 232 maximum and p_2 give us the width of the ThS curve.

233 In the absence of external signals (cosmic rays, injected signals, etc) these noise ThS curves
 234 show the convolution of the envelope of the electronic noise at the output of the fast shaper (the

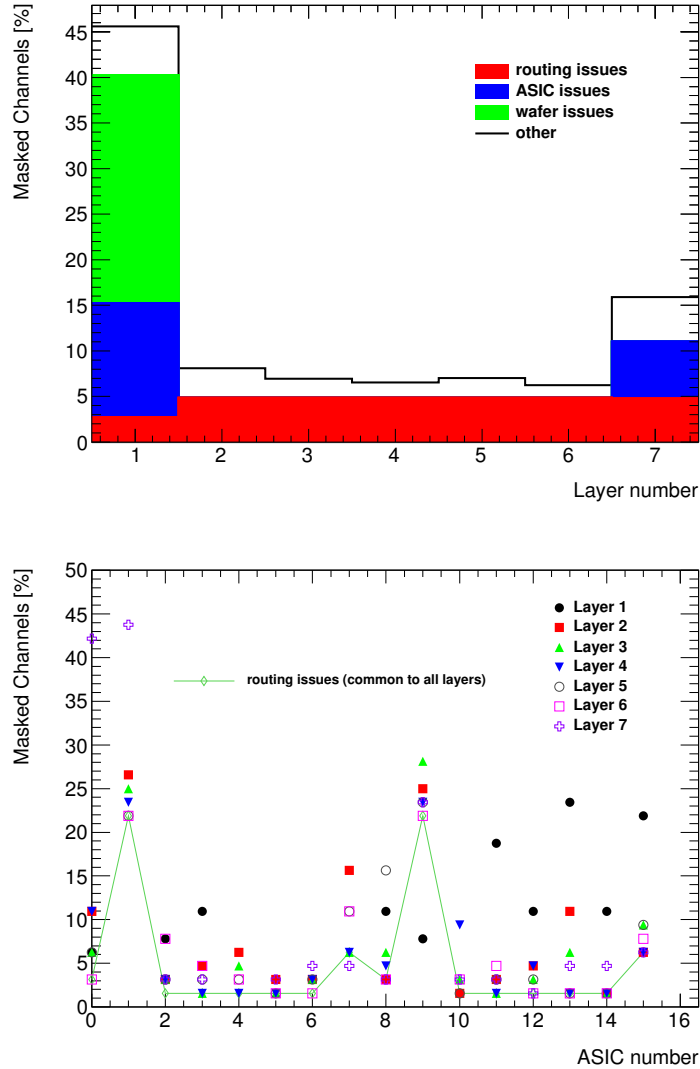


Figure 5. Ratio of channels that are marked as noisy in all slabs. Top: inventory of the different type of noisy channels per slab. Bottom: break down of the total number of noisy channels per ASIC. The ASICs 4-7 (wafer issue) and 10 from layer 1 and the ASIC 4 from layer 7 are not included in the second plot since they are fully masked.

trigger decision branch on the SKIROC). Indeed, the size of this envelope is related to the slow clock frequency.

To reduce to the minimum the presence of cosmic rays signals, we perform runs with short open acquisition windows as described in the previous section. In Figure 6 two result of two threshold scans and the fit by a ThS curves for two different channels from the second layer of the setup are shown.

The function from equation 3.1 was fitted to all channels data and all the values of p_1 and p_2 were saved. The final threshold value of every ASIC, in DAC units, was chosen by taking the

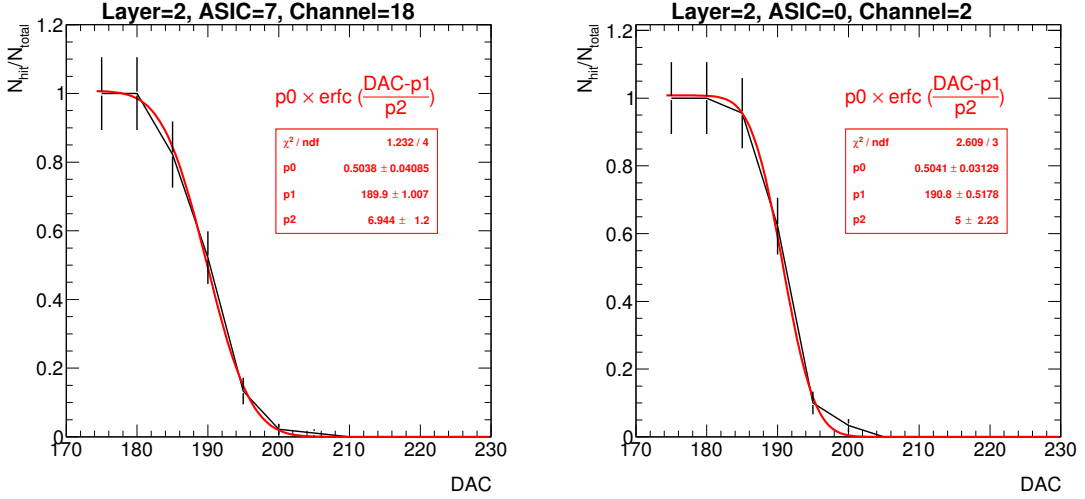


Figure 6. Two threshold scan curves and their associated ThS curves.

$$\text{maximum}(\text{DAC}_{\text{optimal}}^{\text{ASIC}-j} = \langle p_1^{\text{ASIC}-j} \rangle + 5 \times \langle p_2^{\text{ASIC}-j} \rangle, 230) \quad (3.2)$$

if at least the the 30% of the 64 channels ThS curves in the ASIC could be fitted. If only less than the 30% of curves of the 64 channels were successfully fit, a global DAC value of 250 was set. The $\langle \rangle$ denotes the average over all the channels on the ASIC. The choice of these two values was sustained by previous experiences, see for example [27].

The optimal trigger threshold values for all ASICs are shown in Figure 9.

3.3 S/N ratio in the trigger line

Similar kind of measurements can be done but using external signals. This will allow to calculate the signal over noise (S/N) ratio to trigger 1 MIP signals. To calculate the S/N of the trigger we need to compare the 1 MIP ThS curve and 2 MIP ThS curve. The S/N will be defined as the ratio between the distance of both ThS curves at its 50% and the width of the ThS curve.

In Figure 7 we see the 1 MIP and 2 MIP ThS curves obtained for several channel in a SKIROC testboard in which a single SKIROC2 in BGA package is placed and the 1 MIP and 2 MIPs signals are directly injected in the preamplifier (via a 3 pF capacitor located in the injection line as shown in Figure 1). From this plot we can extract a S/N ratio of ~ 12.8 . We do not expect large differences with the results that we would obtain with a full equipped SLABs although this board is thought for commissioning and test of the SKIROC ASICS in an "ideal" environment in contrast with the FEV ASUS that are optimized to meet the detector requirement and to hold several ASICs at the same time.

We have obtained similar results using real signals, in this case cosmic rays signals by using very long acquisition windows of 150 ms at 5 Hz. This is shown in Figure 8 where we show the result of the fit to the noise ThS curves for all channels individually (in red) in one of the ASICs of the second layer together with the results of the ThS curve obtained with cosmic rays integrated for all channels (black points and blue line). We expect a broader distribution of the cosmic ThS

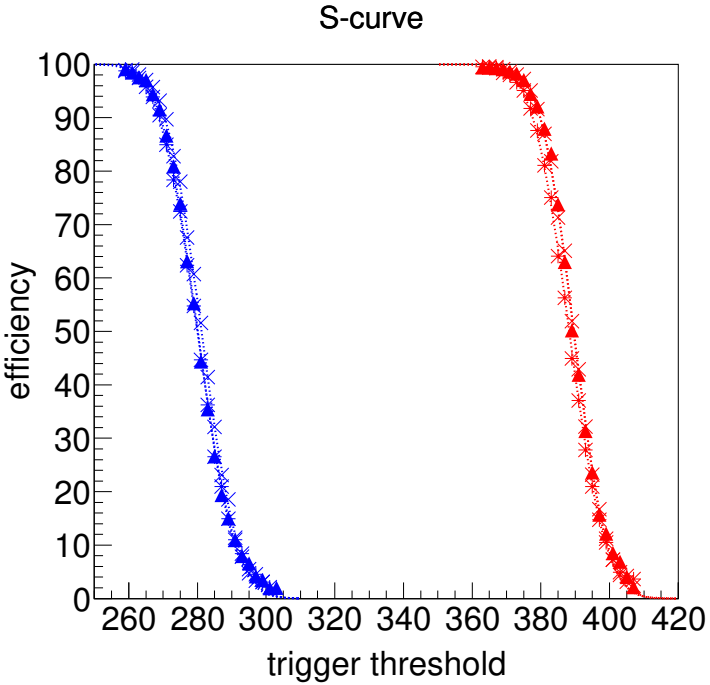


Figure 7. ThS curves with charge injection (1 MIP in blue and 2 MIPs in red) for two different channels in a SKIROC2 testboard. From this plot, we extract a $S/N = 12.8$ in the trigger line.

curve since muons can traverse the detector at different incidence angles. In addition to this, we should remember that the noise ThS curve do correspond to the real noise distribution but only to the envelope of the noise in the fast shaper, therefore the distance between the two ThS curves is smaller than the real distance between noise and signal. Therefore, if we calculate the S/N using this plot, the value would be unrealistic but at least provides the comparison between the ThS curve for 1 MIP real and injected signals.

Both ways of estimating the S/N ratio of the trigger have their own limitations and dedicated studies in beam test are needed in order to precisely determine it. In the meanwhile, combining the information contained in the Figs 7 and 8, we can estimate the value in energy at which we have set our trigger threshold. This is shown in Figure 9.

3.4 Prospects

All the commissioning procedure described above relies in very conservative decisions due to the presence of unknown noise sources during most of the commissioning phase. These sources are now well known and isolated and therefore a new “noise commissioning procedure” has been studied. It will consist in an iterative algorithm that first will identify and mask the channels giving underflowed signals and afterwards run a set of acquisitions in which the number of triggers per channel will be compared with the number of expected triggers assuming only cosmic rays as signal. This will allow us to have an unambiguous definition of the noise levels channel per channel instead of defining such levels relatively to the total number of recorded triggers per ASIC. Finally, once

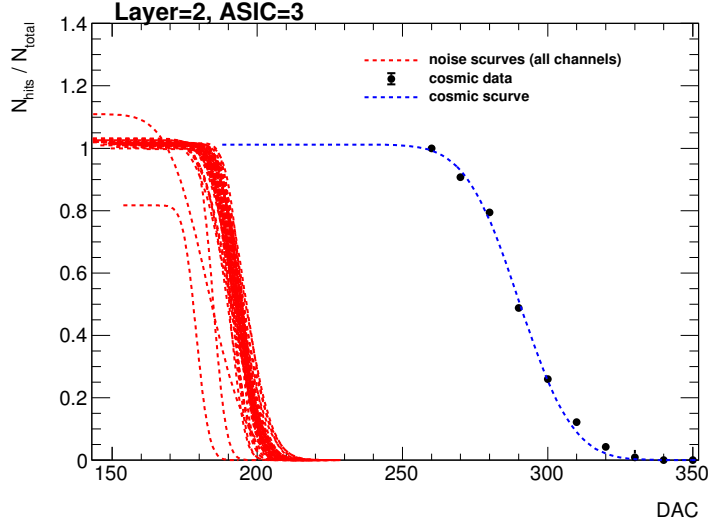


Figure 8. ThS curves for noise (channel by channel, only the result of the fit) and cosmic rays (all channels together) for one ASIC in layer 2.

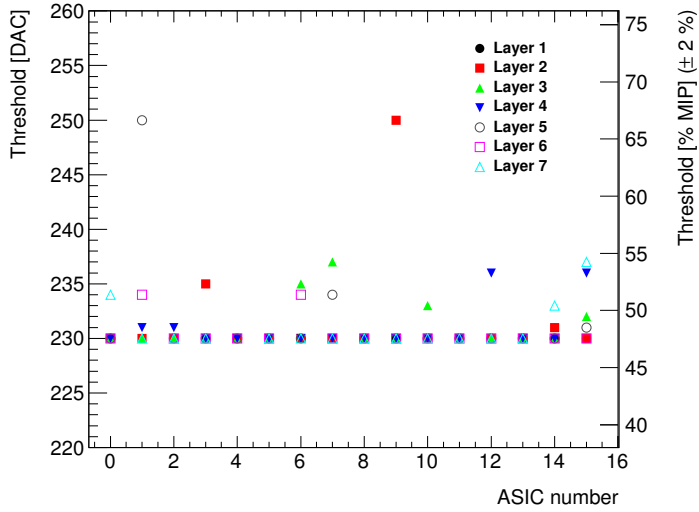


Figure 9. Summary of the trigger threshold settings in internal DAC units and in MIP units.

that the noisy channels are identified, the optimization of the threshold levels will be performed and a last run for identification of noisy channels will be taken using this optimal threshold.

Using this new procedure we manage to reduce the number of masked channels by a factor 2 without any loss of performance, at least in the laboratory and using 3 of the 7 SLABS. This new procedure will be tested in the next beam test. Also, in order to optimize the commissioning of the detector, we propose a new set of measurements in the next beam test such as a scan of optimal delay of the hold values of the trigger using MIP like particles and a threshold scan for the determination of the S/N in the trigger line. This later can be done by the comparison of ThS curves taken with 1

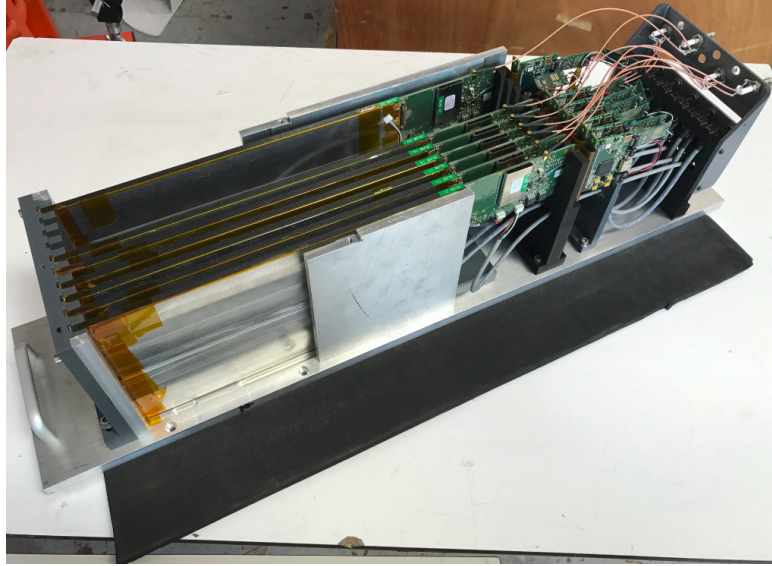


Figure 10. Prototype with 7 layers inside the aluminum stack.

293 MIP and $\sqrt{2}$ MIP signals (tilting the detector by 45 degrees).

294 **4 Performance on positron beam test at DESY**

295 The beam test line at DESY provides continuous positron beams in the energy range of 1 to 6 GeV
 296 with rates from few hundreds of Hz to few KHz with a maximum of \sim 3 KHz for 2-3 GeV. The
 297 particles beam ies produced as follows: first, the electron/positron synchrotron DORIS II is used to
 298 produced a photon beam via bremsstrahlung when interacting with a carbon fiber target; secondly,
 299 these photons are then converted to electron/positron pairs; and, finally, the beam energy is selected
 300 with dipole magnets and collimators. In addition, DESY gives acces to a bore 1 T solenoid, the
 301 PCMag.

302 A photograph showing the SiW-ECAL technollogical prototype setup can be seen in Figure
 303 10. Current prototype consists on 7 layers of SLABs housed by a PVC and aluminum structure
 304 that can hold up to 10. For the beam test described in Section 4 all the layers were separated by
 305 equal distances of 15 mm except the last one which was at 60 mm of its nearest. In the following
 306 sections, we will refer to layers number 1 to 7, where the 1 is the closest to the beam pipe and 7 is
 307 the farthest. The detector was exposed to a positron beam in the DESY test beam area (line 24). By
 308 means of an external pulse generator we defined the length of the acquisition window to be 3.7 ms
 309 at a frequency of 5 Hz. The detector was running in power pulsing mode without any extra active
 310 cooling system.

311 The physics program of the beam test can be summarized in the following points:

- 312 1. Calibration without tungsten absorber using 3 GeV positrons acting as minimum ionizing
 313 particle (MIPs) directed to 81 position equally distributed over the modules.
- 314 2. Test in magnetic field up to 1 T using the PCMag. For this test a special PVC structure was
 315 designed and produced to support one single SLAB. The purpose of such test was twofold:

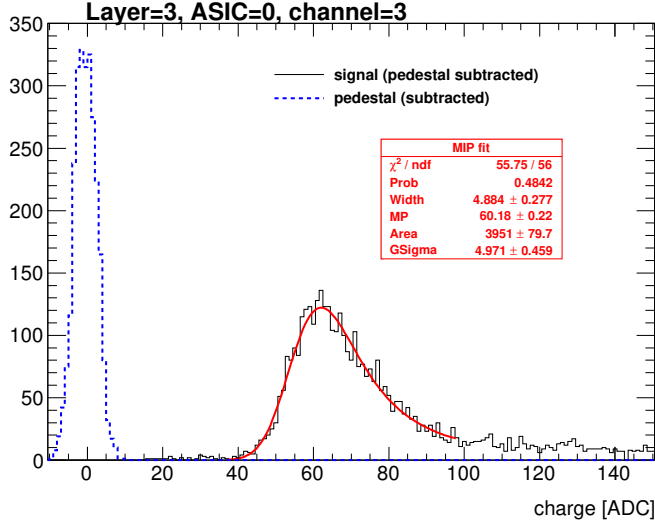


Figure 11. Pedestal (blue dashed line) and signal (black continuous line) distribution for one channel in the third layer.

first to prove that the DAQ, all electronic devices and the mechanical consistency of the SLAB itself are able to handle strong magnetic fields; second to check the quality of the data and the performance of the detector during the data taking when running in a magnetic field.

3. Response to electrons of different energies with fully equipped detector, i.e. sensitive parts and W absorber, with three different repartitions of the absorber material:

- W-configuration 1: 0.6, 1.2, 1.8, 2.4, 3.6, 4.8 and 6.6 X_0
- W-configuration 2: 1.2, 1.8, 2.4, 3.6, 4.8, 6.6 and 8.4 X_0
- W-configuration 3: 1.8, 2.4, 3.6, 4.8, 6.6, 8.4 and 10.2 X_0

First reports on this beam test can be find in Refs. [30, 31]. In this paper we discuss in more detail the results of the pedestal, noise and MIP calibration in Section 4.1. We show also results on the pedestal and noise stability when running inside a magnetic field in Section ???. Finally, a first peek to the response and stability of the detector in electromagnetic showers events is discussed in Section 4.3.

4.1 Response to MIP-acting positrons

4.1.1 Pedestal and noise determination

The calibration runs have been used to calculate the pedestal distribution reference values and the noise levels (the width of the pedestal distribution) of each channel. In Figure 11 we show the signal and pedestal distribution of a single channel after subtracting the pedestal mean position. The results of the MIP calibration fit are included (red) and explained in the next version. The pedestal distribution is shown only for the first SCA to keep the y-axis within a reasonable range. The signal distribution is integrated over all SCAs.

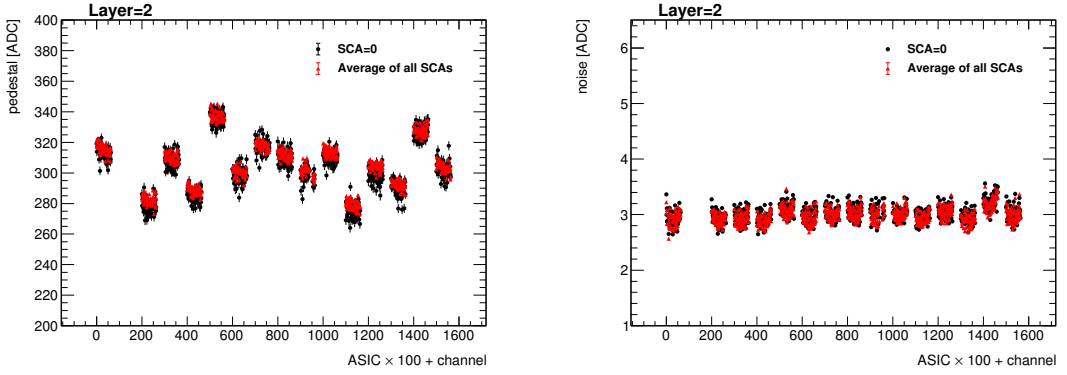


Figure 12. Pedestal mean position (upper plot) and width (lower plot) for all channels in one layer. The data is grouped on bunches in which the value in the x-axis corresponds to the value of the channel number plus the value of the ASIC number multiplied by 100. The black points show the value for the first SCA and the red points show the average value for all the others SCAs (with the standard deviation of the sample as error bar).

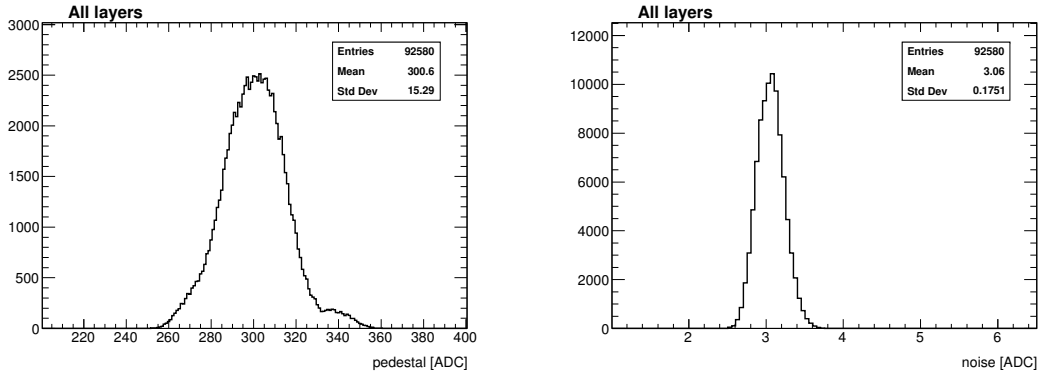


Figure 13. Pedestal mean position (left) and width (right) for all channels and all SCAs in the setup.

337 The pedestal is calculated as the mean position of the ADC distribution of channels without
 338 trigger. The noise is associated to the width of such distribution. The pedestal correction is done
 339 layer-, chip-, channel- and SCA-wisely due to the large spread of values between pedestals, as
 340 observed in Figure 12 (left plot) and Figure 13 (also left plot). For the noise, the dispersion is much
 341 smaller ($\sim 5\%$). This is shown in the right plots of Figures 12 and 13. From now on, the pedestal
 342 correction is applied to all the results presented.

343 4.1.2 Energy calibration and tracking efficiency

344 A Landau function convoluted with a Gaussian is fit to the resulting hit distribution. The most-
 345 probable-value of the convoluted function is taken as the MIP value, allowing thus for a direct
 346 conversion from ADC units to energy in MIP units. We have obtained a raw energy calibration
 347 spread of the 5% among all channels with the 98% of all available channels being fitted. Results
 348 are summarized in figure 14, leftmost plot.

349 We checked the MIP calibration in all calibrated channels by selecting tracks incident perpen-

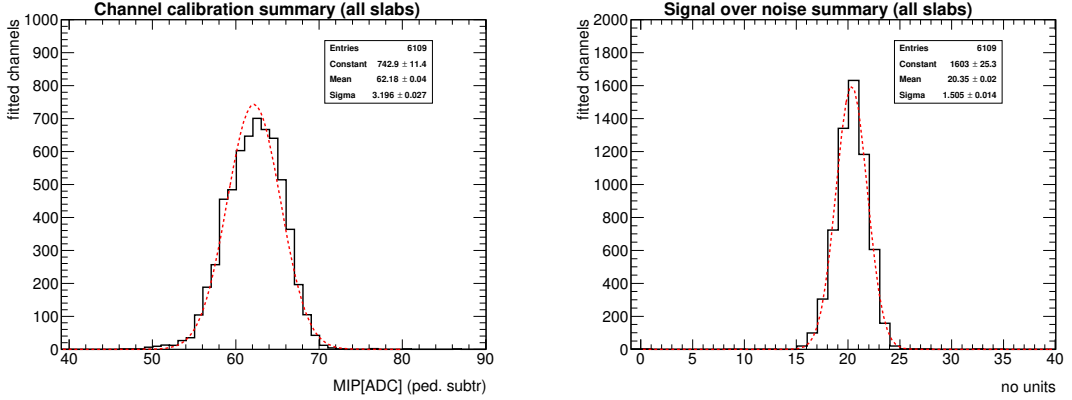


Figure 14. Result of the MIP position calculation and signal over noise calculation for all calibrated channels.

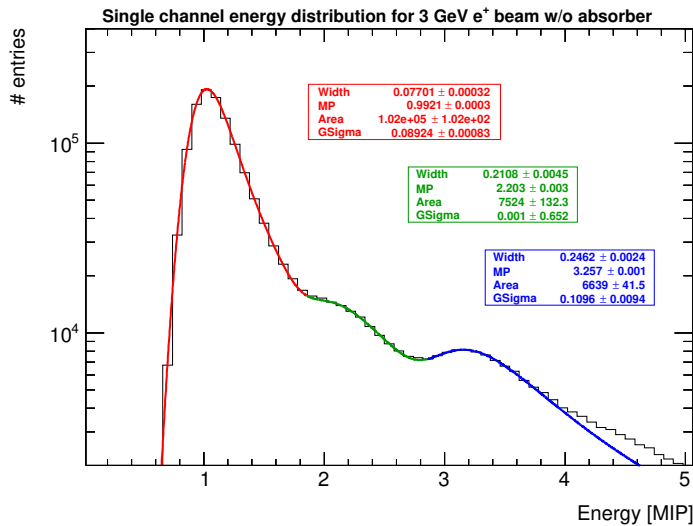


Figure 15. Energy distribution for all calibrated channels when selecting tracks of 3 GeV positron acting as MIPs.

diculary to the layers surface. The results are shown in figure 15 where the single channel energy distribution for MIPs is shown for all calibrated channels in the same distribution. The maximum peaks at 1 MIP as expected after a good calibration. In addition to this, a second and a third peak appear visible. These peaks are due to events involving multiple particles crossing the detector.

To evaluate the single hit detection efficiency we define a high purity sample of events by selecting tracks with at least 4 layers with a hit in exactly the same channel. Afterwards we check if the other layers have or not a hit in the same channel (expanding the search to the closest neighbouring channels) with energy larger or equal than 0.3 MIP. Finally, we repeat this for all layers and channels. The results are shown in Figure 16. Except few exceptions, the efficiency is compatible with 100%. Lower efficiencies in the first layer are related to the presence of noisy channels not spotted during the commissioning. In the last layer (separated from the other layers by four slots of 1.5 cm instead of only one) we also observe few small deviations from the $\sim 100\%$

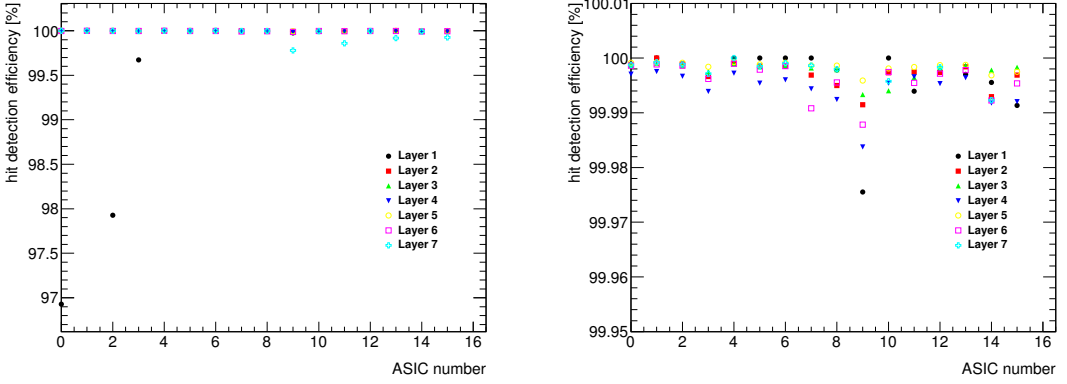


Figure 16. Left: MIP detection efficiency for all layers and ASICs in high purity samples of tracks of MIP-like acting particles. Right: same figures with a zoom in the y-axis. In both cases, the average efficiency of the 64 channels in each ASIC is shown.

which are indeed associated to a slight misalignment of the detector. If we remove these channels from the analysis the full efficiency is recovered.

4.1.3 S/N ratio in the charge measurement for MIP interactions

The signal-over-noise ratio in the charge measurement (corresponding to the slow shaper of the SKIROC2) is defined as the ratio between the most-probable-value of the Landau-gauss function fit to the data (pedestal subtracted) and the noise (the pedestal width). This quantity has been calculated for all channels and all layers. The average S/N is to 20.4. Results are summarized in Figure 14, rightmost plot.

4.2 Pedestal and noise stability in a magnetic field

The data taking inside the magnetic field has been divided in three steps: a) a with a magnetic field of 1 T; b) a run with 0.5 T; c) a final run with the magnet off. The beam, 3 GeV positrons, was hitting in the area of the PCB readout by the ASIC number 12.

The pedestal positions and noise levels of the channels of the ASIC 12 when the SLAB is inside of the PCMag are compared with the results from the calibration run described in the previous section. This is shown in Figure 17. We see that the agreement is perfect within the statistical uncertainties. Due to the lower rates in this beam area, the analysis is only done up to few SCAs.

4.3 Pedestal stability in electromagnetic shower events

In this section we discuss the pedestal stability in events with large amount of charge collected by the ASICs, as are the electromagnetic shower events. All the results shown in this section correspond to data taken during the tungsten program, using the W-configuration number 2 when shooting the beam in the area registered by the ASIC 12 (and partially in the 13). Only information recorded by ASIC 12 is used in the analysis. For other configurations we get comparable results. In order to select a high purity of electromagnetic shower like the events, we used a simple criteria: select only events with at least 6 of the layers with at least a hit with $E > 0.5$ MIP.

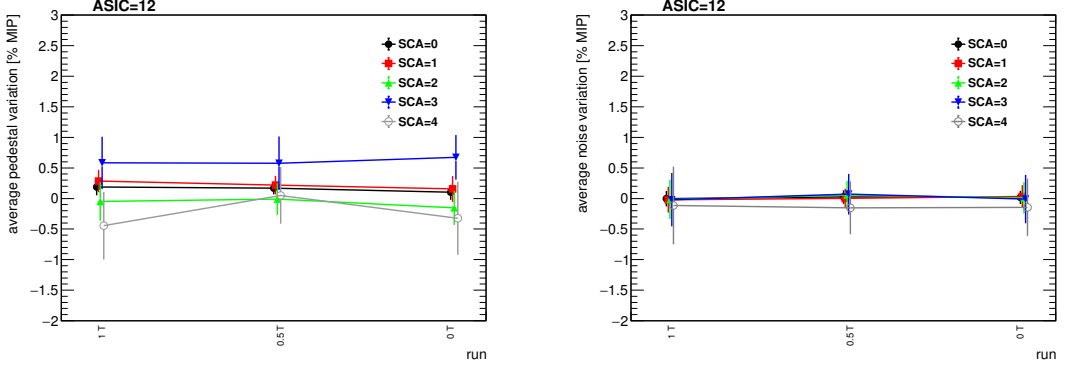


Figure 17. Average deviation of the pedestal mean position (left) and width (right) for all channels in the ASIC 12.

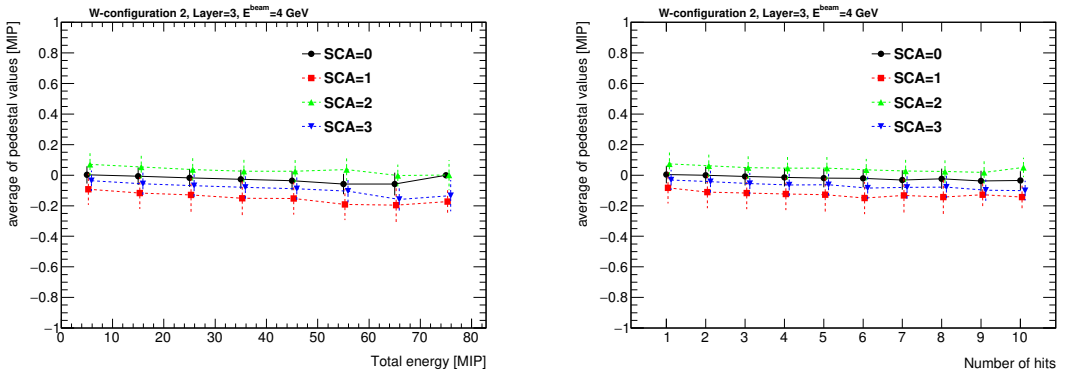


Figure 18. Left: mean position of the projection of the pedestal distribution of all channels calculated when different energies are collected in the ASIC (in bins of 10 MIPs). Right: same but as a function of the number of hits. In both cases, the results are shown for few SCAs. The points for the curves with SCA larger than zero are slightly shifted in the x-axis to optimize the visualization.

387 Two main observations have been extracted from the recalculation of the pedestals and its
 388 comparison with the values obtained previously during the calibration runs. The first observation
 389 consists in a relatively small drift of the pedestal values towards lower values when the collected
 390 energy is high (or when the number of triggered channels is large). This is shown in Figure 18 for
 391 several SCAs where the average of the projection of the pedestal distribution for all channels non
 392 triggered in ASIC 12 of layer 3 is plot as a function of the total energy measured by the ASIC (or
 393 the total number of hits). We see that in both cases, the shapes of the curves for each SCA are very
 394 similar. This feature is known and it is due to the architecture of the SKIROC2 ASICs where high
 395 inrush of currents can slightly shift the baseline of the analogue power supply.

396 The second observation extracted from this analysis can be also seen in Figure 18 but more
 397 clearly in Figure 19: in addition to the small drift of the pedestal value an SCA-alternate global
 398 shift is observed. We see that the effect is enhanced when large amounts of charge are deposited
 399 in the ASIC (*i.e.* at larger beam energies or for the layers in the maximum of the shower profile).
 400 We also observed that this alternation is only SCA dependent and does not depends on the time in

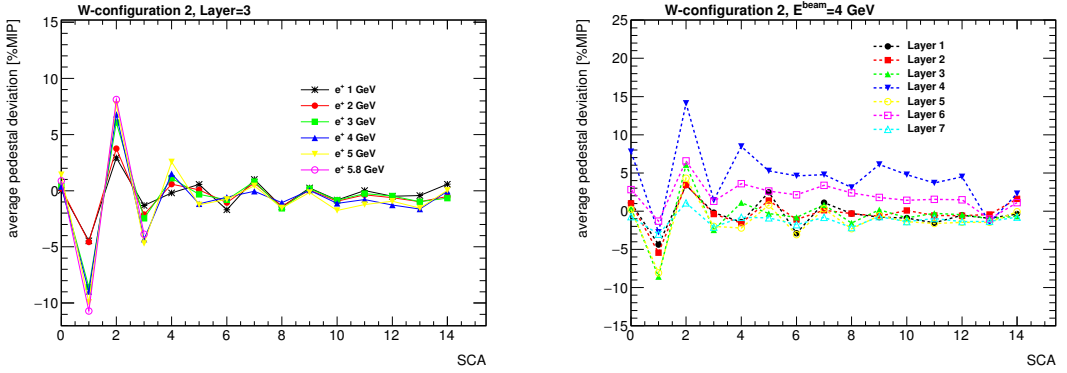


Figure 19. Left: average value on each SCA of the calculated pedestals for all channels of ASIC 12 in the Layer 3 for different energies of the beam. Right: same but fixing the energy of the beam and comparing several layers.

401 which the deposit of energy occurs within the acquisition. This is not yet fully understood although
 402 the fact that the effect is observed in alternate SCAs hints that something is affecting to the digital
 403 part of the ASIC (where the SCAs enter in play). Dedicated tests in the laboratory and in the beam
 404 are needed in order to clarify this issue.

405 5 Summary

406 The R&D program of the highly granular SiW-ECAL detector is in an exciting phase. After the
 407 proof of principle of the imaging calorimetry concept using the physics prototype, the technological
 408 prototype is being constructed and tested. In this document we describe the commissioning and
 409 beam test performance of a prototype built in with the first fully assembled detector elements.

410 A very comprehensive and detailed commissioning procedure has been established and opti-
 411 mized allowing us to identify and isolate the different noise sources that could spoil the data taking.
 412 The beam test has provided a lot of useful data to study the performance of the detector and to
 413 perform a channel by channel calibration. A full analysis of the MIP calibration within magnetic
 414 field and the response of the prototype in electromagnetic shower events will be covered in a future
 415 document. In addition, the results shown here serve as input for ongoing and future R&D.

416 6 Outlook

417 In parallel to the work described here, several R&D efforts are being carried. One of these efforts
 418 is directed to the design and test of new ASICs. In fact, a new generation of SKIROC2, the 2a,
 419 has been delivered and it is being tested in the dedicated testboards and it has been integrated in
 420 new ASUs. In addition, a new generation of the ASIC, SKIROC3, is foreseen for the final detector
 421 construction. In contrast with SKIROC2/2a, the new ASIC will be fully optimized for ILC operaton,
 422 *i.e.* full zero suppression, reduced power consumption etc.

423 Many efforts are also concentrated in the construction and test of long SLABs made of several
 424 ASUs enchainied since we know that the ILD ECAL will host long layers of up to $\sim 2.5\text{m}$. This

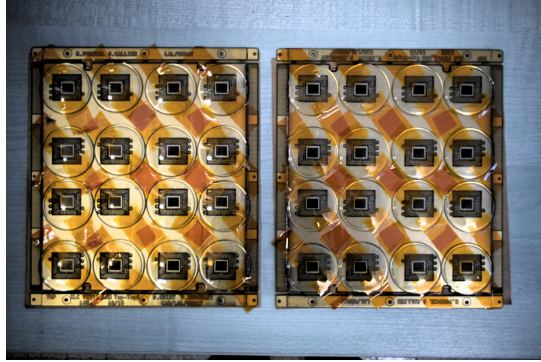


Figure 20. Two FEV11_COB boards with 16 SKIROC2a wire bonded. The ASICS are protected with watch glasses.

device constitutes a technological challenge in both aspects, the mechanical (very thin and long structure with fragile sensors in the bottom, complicated assembly procedure...) and the electrical (i.e. transmission of signals and high currents). For example, interconnections between ASUs and between ASU and interface card are one of the most involved parts of the assembly and require close collaboration between mechanical and electronic engineers. The construction and test of a long SLAB prototype of ~ 8 ASUs is currently ongoing.

In parallel to the ASUs equipped with BGA packaged ASICS, a different proposal for the ASU design is being investigated. This is motivated by the high density of channels demanded by the Particle Flow algorithms. Indeed, the FEV11 thickness is 1.6 alone and 2.7 mm including the ASICS in its current packaging: 1.1 mm thick LFBGA package. In this alternative PCB design the ASICS are directly placed on board of the PCB in dedicated cavities. The ASICS will be in semiconductor packaging and wire bonded to the PCB. This is the so-called COB (chip-on-board) version of the ASU. A small sample of FEV11_COBs (same connexion pattern with the interface card than FEV11) with a total thickness of 1.2 mm allowing for a potential denisty of 10000 channels/dm³ has been produced and tested in the laboratory showing its readiness for tests with particle beams.

A sample can be seen in Figure 20.

Finally, many efforts in the compactification of the DAQ and the ASUs (*i.e.* the chip on board versions of the ASUs described in Section 2.3) are being conducted by the SiW-ECAL collaboration.

It is foreseen that all these developments, with the exception of the SKIROC3, will be tested with particle beams during 2018-2019.

445 Acknowledgments

This project has received funding from the European Union's Horizon 2020 Research and Innovation program under Grant Agreement no. 654168. This work was supported by the P2IO LabEx (ANR-10-LABX-0038), excellence project HIGHTEC, in the framework 'Investissements d'Avenir' (ANR-11-IDEX-0003-01) managed by the French National Research Agency (ANR). The research leading to these results has received funding from the People Programme (Marie Curie Actions) of the European Union's Seventh Framework Programme (FP7/2007-2013) under REA grant agreement, PCOFUND-GA-2013-609102, through the PRESTIGE programme coordinated by Campus France.

453 The measurements leading to these results have been performed at the Test Beam Facility at DESY
454 Hamburg (Germany), a member of the Helmholtz Association (HGF).

455 A Apéndice: Filtering of fake triggers

456 Several types of fake signals have been observed in the technological prototype since its construction
457 and test. A detailed description of them can be found in previous articles, as for example, in Ref.
458 [27]. All these fake signals are easily identified and tagged during the data acquisition and removed
459 afterwards from the analysis not introducing any significance loss of performance as can be seen,
460 for example, in the hit detection efficiency plots (see Section 4.1.2). In the following, we briefly
461 describe the status of the monitoring, debugging and filtering of such kind of events.

462 Empty triggers

463 Empty trigger events are a well known feature of SKIROC2. The SKIROC2 uses an OR64 signal
464 to mark the change to a new SCA when a signal over threshold is detected. The empty triggers
465 appear when during the acquisition the rising edge of the slow clock falls during the OR64 signal
466 and therefore the change to a new SCA is validated twice. This effect creates around 10-15% of
467 empty events which are easily filter and removed from the analysis. **The ratio of empty triggers in**
468 **the new SKIROC2a is reduced to the ~ 3% thanks to to a decrease of the OR64 size by a factor X.**

469 Plane events and retriggers

470 Another well known issue is the appearance of bunches of consecutive fake triggers, called retriggers,
471 that saturates the DAQ. These events are also characterized by triggering many channels (some times
472 even all channels of an ASIC) at the same time. Although the ultimate reason of the appearance of
473 these events remains unknown we think that they may be related to some distortion of the power
474 supply baselines. We know that the SKIROC2 and 2a preamplifiers are referenced to the analog
475 power supply level, therefore, any voltage dip can be seen as signal by the preamplifiers. The
476 presence of a high inrush of current due to many channels triggered at the same time can create
477 these voltage dips and produce the so called plane events (most of the channels triggered at once).
478 In previous studies (*i.e.* reference [27]), the ratio of retriggers and plane events was reduced by
479 improving the power supply stabilization capacitances. It is important to remark that all layers and
480 all ASICs analog and digital levels are powered using the same power supply. Moreover, the high
481 voltage power supply for the polarization of the PIN diode it is also common for all layers. Therefore
482 any noise in these power supplies or any overload of an ASIC may participate in the creation of fake
483 signals in different ASICs and layers.

484 Studying the MIP calibration data of this beam test we have noticed that the larger concentration
485 of the retriggers and plane events are originated in ASICs far from the beam spot. Even more, hot
486 spots tend to appear near the channels 37 and the channels masked as suspicious of suffering from
487 routing issues. The amount these events have been estimated to be of 1 – 3% in the ASICs where
488 high frequency interactions are produced (*i.e.* using 3 GeV positrons at 2-3 KHz) and at higher
489 rates even larger than 40% in other ASICs far from the beam spot. Moreover, it has been noticed a
490 correlation between the time that an ASIC was full and the time of the appearance of some retriggers
491 in other areas of the PCB. This correlation corresponds to ~1.6 μ s which hints of a distortion on

492 the analogue power supply when the signal that informs the DIF that one ASIC memory is full is
493 transmitted through the PCB.

494 All this information and dedicated studies in the laboratory will be used for the improvement
495 of the power supplying system, the PCB design and for further SKIROC developments with the
496 possible approval the ILC in the scope.

497 References

- 498 [1] T. Behnke, J. E. Brau, B. Foster, J. Fuster, M. Harrison, J. M. Paterson et al., *The International Linear
499 Collider Technical Design Report - Volume 1: Executive Summary*, [1306.6327](#).
- 500 [2] H. Baer, T. Barklow, K. Fujii, Y. Gao, A. Hoang, S. Kanemura et al., *The International Linear
501 Collider Technical Design Report - Volume 2: Physics*, [1306.6352](#).
- 502 [3] C. Adolphsen, M. Barone, B. Barish, K. Buesser, P. Burrows, J. Carwardine et al., *The International
503 Linear Collider Technical Design Report - Volume 3.I: Accelerator & in the Technical Design Phase*,
504 [1306.6353](#).
- 505 [4] C. Adolphsen, M. Barone, B. Barish, K. Buesser, P. Burrows, J. Carwardine et al., *The International
506 Linear Collider Technical Design Report - Volume 3.II: Accelerator Baseline Design*, [1306.6328](#).
- 507 [5] H. Abramowicz et al., *The International Linear Collider Technical Design Report - Volume 4:
508 Detectors*, [1306.6329](#).
- 509 [6] M. Aicheler, P. Burrows, M. Draper, T. Garvey, P. Lebrun, K. Peach et al., *A Multi-TeV Linear
510 Collider Based on CLIC Technology*, .
- 511 [7] L. Linssen, A. Miyamoto, M. Stanitzki and H. Weerts, *Physics and Detectors at CLIC: CLIC
512 Conceptual Design Report*, [1202.5940](#).
- 513 [8] P. Lebrun, L. Linssen, A. Lucaci-Timoce, D. Schulte, F. Simon, S. Stapnes et al., *The CLIC
514 Programme: Towards a Staged e+e- Linear Collider Exploring the Terascale : CLIC Conceptual
515 Design Report*, [1209.2543](#).
- 516 [9] J.-C. Brient and H. Videau, *The Calorimetry at the future e+ e- linear collider*, *eConf C010630*
517 (2001) E3047, [[hep-ex/0202004](#)].
- 518 [10] V. Morgunov and A. Raspereza, *Novel 3-D clustering algorithm and two particle separation with tile
519 HCAL*, in *Linear colliders. Proceedings, International Conference, LCWS 2004, Paris, France, April
520 19-23, 2004*, pp. 431–436, 2004. [physics/0412108](#).
- 521 [11] F. Sefkow, A. White, K. Kawagoe, R. Pöschl and J. Repond, *Experimental Tests of Particle Flow
522 Calorimetry*, *Rev. Mod. Phys.* **88** (2016) 015003, [[1507.05893](#)].
- 523 [12] CALICE collaboration, C. Adloff, J. Blaha, J. J. Blaising, C. Drancourt, A. Espargiliere, R. Galione
524 et al., *Tests of a particle flow algorithm with CALICE test beam data*, *JINST* **6** (2011) P07005,
525 [[1105.3417](#)].
- 526 [13] CALICE collaboration, J. Repond et al., *Design and Electronics Commissioning of the Physics
527 Prototype of a Si-W Electromagnetic Calorimeter for the International Linear Collider*, *JINST* **3**
528 (2008) P08001, [[0805.4833](#)].
- 529 [14] CALICE collaboration, C. Adloff et al., *Response of the CALICE Si-W electromagnetic calorimeter
530 physics prototype to electrons*, *Nucl. Instrum. Meth. A* **608** (2009) 372–383, [[0811.2354](#)].
- 531 [15] C. Adloff et al., *Study of the interactions of pions in the CALICE silicon-tungsten calorimeter
532 prototype*, *JINST* **5** (2010) P05007, [[1004.4996](#)].

- 533 [16] CALICE collaboration, C. Adloff et al., *Effects of high-energy particle showers on the embedded*
 534 *front-end electronics of an electromagnetic calorimeter for a future lepton collider*, *Nucl. Instrum.*
 535 *Meth. A* **654** (2011) 97–109, [[1102.3454](#)].
- 536 [17] CALICE collaboration, B. Bilki et al., *Testing hadronic interaction models using a highly granular*
 537 *silicon–tungsten calorimeter*, *Nucl. Instrum. Meth. A* **794** (2015) 240–254, [[1411.7215](#)].
- 538 [18] GEANT4 collaboration, S. Agostinelli et al., *GEANT4: A Simulation toolkit*, *Nucl. Instrum. Meth.*
 539 *A* **506** (2003) 250–303.
- 540 [19] J. Allison et al., *Geant4 developments and applications*, *IEEE Trans. Nucl. Sci.* **53** (2006) 270.
- 541 [20] J. Allison et al., *Recent developments in GEANT4*, *Nucl. Instrum. Meth. A* **835** (2016) 186–225.
- 542 [21] CALICE collaboration, R. Cornat and R. Pöschl, *Technological prototype of a silicon-tungsten*
 543 *imaging electromagnetic calorimeter*, *JINST* **10** (2015) C06015.
- 544 [22] CALICE collaboration, R. Cornat, *Semiconductor sensors for the CALICE SiW EMC and study of the*
 545 *cross-talk between guard rings and pixels in the CALICE SiW prototype*, *J. Phys. Conf. Ser.* **160**
 546 (2009) 012067.
- 547 [23] S. Callier, F. Dulucq, C. de La Taille, G. Martin-Chassard and N. Seguin-Moreau, *SKIROC2, front*
 548 *end chip designed to readout the Electromagnetic CALorimeter at the ILC*, *JINST* **6** (2011) C12040.
- 549 [24] F. Gastaldi, R. Cornat, F. Magniette and V. Boudry, *A scalable gigabit data acquisition system for*
 550 *calorimeters for linear collider*, *PoS TIPP2014* (2014) 193.
- 551 [25] M. Rubio-Roy, F. Thiant and F. Magniette, *Flexible online monitoring for high-energy physics with*
 552 *Pyrame*, *J. Phys. Conf. Ser.* **898** (2017) 032009.
- 553 [26] CALICE collaboration, F. Magniette and A. Irles, *Pyrame 3, an online framework for Calice*
 554 *SiW-Ecal*, *JINST* **13** (2018) C03009.
- 555 [27] M. S. Amjad et al., *Beam test performance of the SKIROC2 ASIC*, *Nucl. Instrum. Meth. A* **778** (2015)
 556 78–84.
- 557 [28] V. Boudry, R. Cornat, D. Lacour, R. Pöschl and F. Magniette, *Advanced assembly chain for Si*
 558 *calorimeters*, .
- 559 [29] T. Suehara et al., *Performance study of SKIROC2/A ASIC for ILD Si-W ECAL*, *JINST* **13** (2018)
 560 C03015, [[1801.02024](#)].
- 561 [30] CALICE collaboration, A. Irles, *Latest R&D news and beam test performance of the highly granular*
 562 *SiW-ECAL technological prototype for the ILC*, *JINST* **13** (2018) C02038, [[1802.08806](#)].
- 563 [31] CALICE collaboration, A. Irles, *Latest developments on the highly granular Silicon-Tungsten*
 564 *Electromagnetic Calorimeter technological prototype for the International Large Detector*, in *2017*
 565 *IEEE Nuclear Science Symposium and Medical Imaging Conference (NSS/MIC 2017) Atlanta,*
 566 *Georgia, USA, October 21-28, 2017*, 2018. [1801.10407](#).